ORIGINAL PAPER

3-D mesoporous nano/micro-structured Fe$_3$O$_4$/C as a superior anode material for lithium-ion batteries

Quanyi Hao · Danni Lei · Xiaoming Yin · Ming Zhang · Shuang Liu · Qiuhong Li · Libao Chen · Taihong Wang

Abstract Urchin-like nano/micro-structured Fe$_3$O$_4$/C composite has been successfully synthesized using inexpensive starting materials. The urchin-shaped nano/micro-structure consisted of several oriented nanorods. TEM analysis revealed that there is a large number of pores and uniform amorphous carbon distribution at a nanoscale in the nanorods walls. As used in lithium-ion batteries, the mesoporous Fe$_3$O$_4$/C anode delivered a higher reversible capacity of about 830 mAh g^{-1} at 0.1 C up to 50 cycles, as well as enhanced high-rate capability compared with urchin-like Fe$_2$O$_3$ and commercial Fe$_3$O$_4$. The improvements can be attributed to the combined effects of the nano/micro-architecture, the porosity, and the ultra-fine carbon matrix, where the three factors would contribute to possess both the merits of nanometer-sized building blocks and micro-sized assemblies and provide high electronic conductivity. It is believed that the results of this study offer new prospects for improving the lithium storage capacity of metal oxides by controlling both architecture and composition.

Keywords Magnetite · Porous · Carbon coating · Anode · Lithium-ion batteries

Q. Hao · D. Lei · X. Yin · M. Zhang · S. Liu · Q. Li ·
L. Chen (✉) · T. Wang (✉)
Key Laboratory for Micro-Nano Optoelectronic Devices
of Ministry of Education, and State Key Laboratory
for Chemo/Biosensing and Chemometrics,
Hunan University,
Changsha 410082, China
e-mail: libao_chen@163.com

T. Wang
e-mail: thwang@hnu.cn

Introduction

Rechargeable lithium-ion batteries (LIBs) have been widely used as power sources for various portable electronic devices such as digital cameras and cellular phones for decades [1–4]. However, they still lie behind the increasing worldwide demands of higher power for applications such as power tools and electric vehicles, due to the low intrinsic capacity of commercial graphite anodes [4–7]. The tremendous challenge has motivated intense interest in designing and developing new electrode materials with higher capacity and cycling stability for next-generation LIBs. Recently, various metal oxides have been investigated extensively as potential alternative anode materials with higher theoretical capacity (500–1,000 mAh g^{-1}) [5, 8–11]. Unfortunately, most of these metal oxides usually suffer from the problems of drastic volume expansion/contraction, and severe particle aggregation associated with the Li ion insertion/extraction process results in fast capacity fading and poor cycling stability consequently, especially at high rates [5, 6, 8, 12]. Although many different approaches have been developed to solve these intractable problems, the reversible capacity, cyclability, and high-rate capability are still disappointing and remain a great challenge.

Among these metal oxides, magnetite (Fe$_3$O$_4$) has been extensively investigated as one of the most promising electrode materials because of its high theoretical capacity (926 mAh g^{-1}), eco-friendliness, and natural abundance [7, 13, 14]. However, a truly durable high capacity and high-rate capability for Fe$_3$O$_4$-based electrodes have rarely been achieved due to problems mentioned above. Recent researches have demonstrated that nanostructure can effectively increase the active reaction sites, accommodate the large volume change, and lead to improved performance.

Nevertheless, nanostructured electrodes also encounter new serious drawbacks, such as large irreversible capacity resulting from the decomposition of electrolyte on active materials, electrode pulverization, and agglomeration associated with low thermodynamic stability [10, 13, 15]. Carbon-coating [17, 18] and porous structure [13, 16–20] have been demonstrated to be beneficial to solve these problems. The former cannot only guarantee good electrical contact but also alleviate the degrading of the electrode, whereas the latter can provide a very short Li ion diffusion pathway, large active surface, as well as local empty space to accommodate large volume change. Besides, it has been reported that developing three-dimensional (3-D) nano/micro-structured electrode materials is also a good choice, which possess both the merits of nanometer-sized materials and micro-sized assemblies (e.g., thermodynamic stability) and exhibit better electrochemical performance [10, 21–25]. For example, Wang et al. [25] demonstrated that 3-D porous-structured Co_3O_4 exhibited high reversible capacity and higher rate capability in LIBs. Furthermore, 3-D porous NiO and 3-D flower-shaped SnO_2 prepared by Wang et al. [10] and Yang et al. [23] also showed enhanced lithium storage performance.

In this paper, we report a facile strategy to synthesize 3-D urchin-like mesoporous Fe_3O_4/C composite as anode material for LIBs, which can efficiently utilize the unique properties of nano/micro-structure, porosity, and carbon-coating to simultaneously address these intractable issues and obtain LIBs with improved performances. Most importantly, by using the composite electrodes, we have demonstrated a high reversible capacity of 830 mAh g^{-1} at 0.1 C over 50 cycles as well as high-rate capacities of 788 mAh g^{-1} at 1 C and 594 mAh g^{-1} at 2 C, suggesting its potential use as anode material for high power LIBs.

Experimental section

Urchin-like α-FeOOH employed as precursor to synthesize Fe_3O_4/C composite was prepared by a simple solution process that was described in our previous reports [26]. $FeSO_4 \cdot 7H_2O$ (1.39 g) and $H_3COONa \cdot 4H_2O$ (1.36 g) were dissolved in 50 ml of deionized water at room temperature. After stirring vigorously for a period at 60°C, the yellow slurry was centrifuged and washed several times with distilled water. Then, the obtained FeOOH precursor was dispersed into 40 ml of glucose solution (20 mg ml^{-1}) by ultrasonication to form a suspension. The resulting suspension was sealed in a 50 ml Teflon-lined autoclave and heated at 180°C for 12 h. The dark brown products were washed and separated by centrifugation–redispersion cycles with deionized water and dried under vacuum at 80°C. For the LIBs tests, the dried products were calcined

at 550°C for 6 h under a nitrogen flow with a heating rate of 4°C min^{-1}.

The crystal structure of the products was determined by X-ray diffraction (XRD, Siemens D-5000) with Cu Kα ($\lambda=$ 1.5418Å). The morphology and structure were investigated by scanning electron microscopy (SEM; Hitachi S-4800) and transmission electron microscope (TEM; JEOL 2010). The porosity analysis was performed through a Micromeritics ASAP 2020 apparatus. The carbon content was determined by thermogravimetric analysis (TGA; Netzsch STA 449C).

Electrochemical measurements were carried out via CR2016 coin-type cells. The working electrodes were prepared by mixing 80 wt.% active material (Fe_3O_4/C composite, commercial Fe_3O_4, or urchin-like Fe_2O_3), 10 wt.% acetylene black (Super-P), and 10 wt.% carboxyl methyl cellulose binder dissolved in distilled water. After coating the above slurries on Cu foil, the electrodes were dried at 120°C under vacuum to remove the solvent. The cells were assembled in an argon-filled glovebox with water and oxygen contents less than 1 ppm. A Celgard 2400 separator, pure lithium foil counter electrode, and 1 M LiPF$_6$ in ethylene carbonate/dimethyl carbonate/diethyl carbonate (1:1:1, in weight percent) were used to fabricate the coin cells. The discharge and charge measurements were carried on an Arbin BT2000 system with the cut-off potentials between 0 and 3 V. The AC impedance spectra of the cells after certain cycles were measured on an electrochemical workstation (CHI 660B) with the frequency range from 0.01 Hz to 100 kHz.

Results and discussion

Structure and morphology

X-ray diffraction (XRD) patterns of the as-prepared FeOOH precursor and Fe_3O_4/C composite are shown in Fig. 1 which match very well with tetragonal α-FeOOH (JCPDS 81-463) and face-centered Fe_3O_4 (JCPDS 85-1436). We found that annealing the carbon-coated FeOOH in an argon atmosphere led to Fe_3O_4 as indicated by the XRD pattern. No diffraction peak corresponding to graphitic carbon is observed in the XRD pattern, showing that the carbon layer is amorphous. The narrow and sharp peaks suggest highly crystalline nature of the obtained Fe_3O_4 product.

The morphology and micro-structure of the samples were examined by scanning electron microscopy (SEM) and transmission electron microscopy (TEM). Figure 2a gives a representative SEM image of the urchin-like α-FeOOH. It can be seen that the samples are uniform urchin-shaped nano/micro-structure with an average diameter of 1 μm. High-magnification SEM image (inset of Fig. 2a) shows that the urchin-like α-FeOOH consists of several
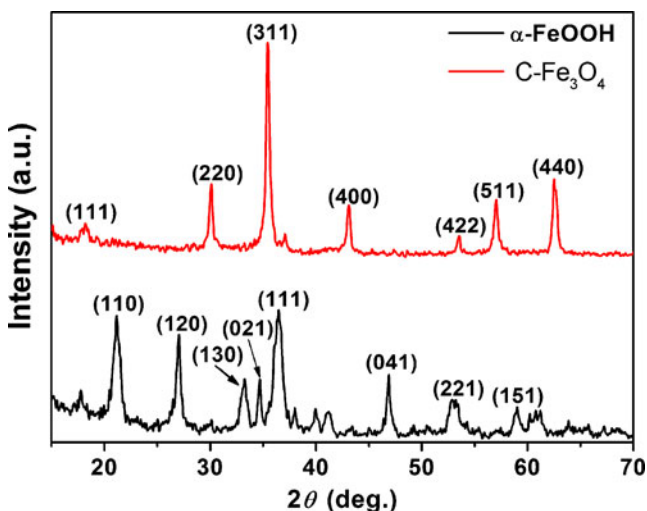
Fig. 1 XRD patterns of urchin-like α-FeOOH and Fe₃O₄/C composite

straight and radially grown nanorods. The diameter of the nanorods is around 30–40 nm (Fig. 3a), and the average length is about 500 nm. Figure 2b displays the SEM image of the Fe₃O₄/C composite; it can be observed that the overall morphology of the FeOOH precursor is perfectly maintained, indicating uniform carbon coatings. The typical TEM images in Fig. 2c and the inset depict that the Fe₃O₄/C building blocks (nanorods) are porous, and the size of the pores distribution is less than 10 nm, which

has been further confirmed by the porosity analysis (Fig. 3b). The release of H_2O and partial reduction of Fe (III) to Fe (II) that occur in the annealing process likely enable the formation of this porous structure. This porosity may promote the diffusion of Li ions in the electrodes, offer a large materials/electrolyte contact area, and accommodate the strain induced by the volume change [1, 19, 27]. The high-resolution transmission electron microscopy (HRTEM) image of the composite is shown in Fig. 2d, the lattice fringes taken from single nanorods are clearly visible with a spacing of 0.25 and 0.46 nm, corresponding to the d-spacing of (311) and (111) planes of Fe_3O_4, respectively. Both the outer amorphous carbon layer and the inner Fe_3O_4 core are visible. The carbon layer with a thickness of 2–5 nm is uniform and continuous. Such a carbon layer serves as the conductive channels and is favorable for stabilizing the electronic and ionic conductivity.

Thermogravimetric analysis (TGA) was used to reveal the chemical composition of the final composite, as displayed in Fig. 3c. The TGA curve displays a first weight loss from 50°C followed by a weight gain between 150°C and 350°C, and then a second weight loss above 350°C. The first weight loss corresponds to the removal of the weakly adsorbed water and other small molecules, and the weight grain corresponds to the transformation of the

Fig. 2 **a** SEM image of urchin-like α-FeOOH (*inset* close views). **b** SEM image of Fe₃O₄/C composite (*inset* close views). **c** TEM image of Fe₃O₄/C composite (*inset* the high-magnification image). **d** HRTEM image of Fe₃O₄/C composite

a

b

c
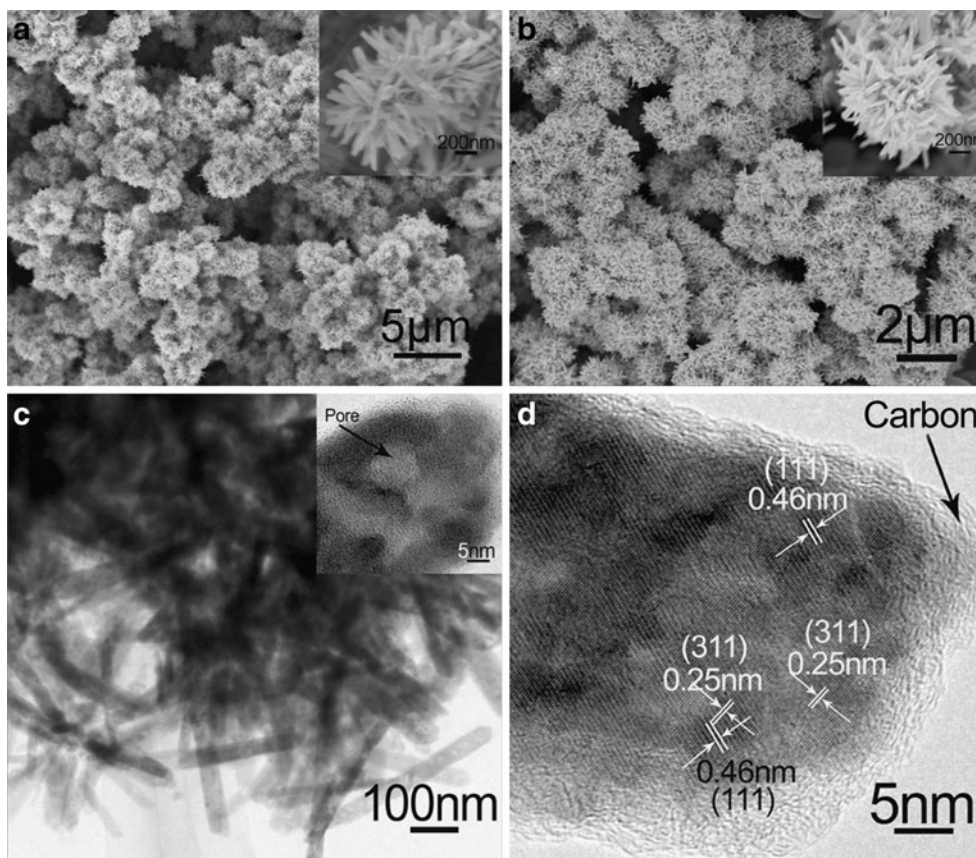
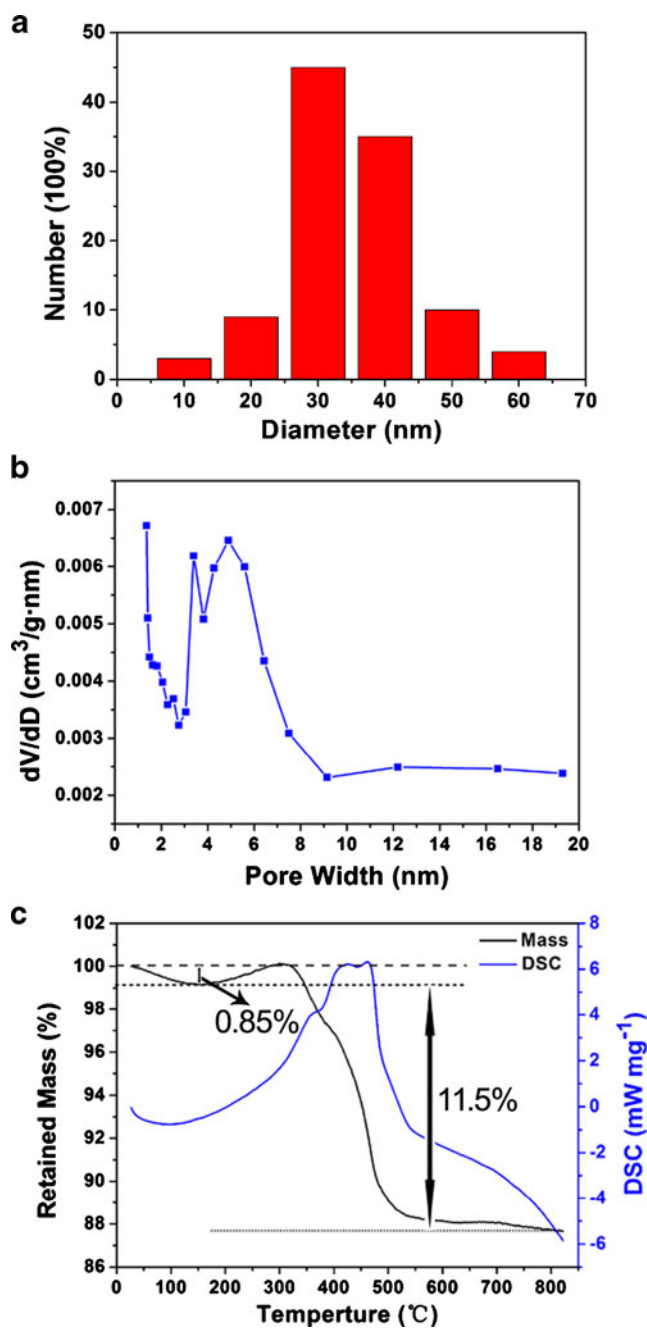**Fig. 3** **a** Statistical nanorod diameter distribution graph of the Fe_3O_4/C composite. **b** Pore size distribution curves of the Fe_3O_4/C composite. **c** TGA and DSC curves of the Fe_3O_4/C composite

magnetite to the maghemite [7, 14], whereas the second weight loss at higher temperature could be mainly attributed to the evaporation and subsequent decomposition of the amorphous carbon layer. Therefore, from the TG analysis, the composite has a chemical composition of 88.5 wt.% Fe_3O_4 and 11.5 wt.% carbon. This leads to a theoretical specific capacity of 862.3 $mAhg^{-1}$ for the Fe_3O_4/C composite.

Electrochemical performances

The Fe_3O_4/C composite exhibits excellent electrochemical performances, which were firstly evaluated by galvanostatic charge/discharge cycling at a current rate of 0.1 C. For comparison, we also tested the electrochemical performances of urchin-like Fe_2O_3 and commercial Fe_3O_4 under the same conditions. The SEM images of the urchin-like Fe_2O_3 and commercial Fe_3O_4 are shown in Fig. 4a, b, respectively. Figure 5 shows the charge/discharge profiles of the urchin-like Fe_2O_3, commercial Fe_3O_4, and Fe_3O_4/C composite electrodes in the first, second, third, and tenth cycles. In the first discharge curve, two obvious plateaus (1.2–0.9 and 0.8 V) are clearly observed for the urchin-like Fe_2O_3 (Fig. 5a), which are similar to those reported for Fe_2O_3 [28, 29]. From the second cycle, only one discharge slope is observed in the range of 1.2–0.8 V. In the cases of the commercial Fe_3O_4 (Fig. 5b), the first discharge curve with only one potential plateau at about 0.8 V and second discharge curve with one plateau between 0.9 and 1.5 V are observed, which are similar to those described for Fe_3O_4 anodes [1, 30]. Compared to the commercial Fe_3O_4, the first discharge curve of the Fe_3O_4/C composite (Fig. 5c) has a different behavior before the conversion plateau at 0.8 V. Specifically, a short plateau-like step at 1.0 V is observed in the first discharge of the Fe_3O_4/C composite electrode. Lithium intercalation into the Fe_3O_4 before the conversion reaction and Li ions consumption resulted from formation of an SEI layer account for this discharge behavior and has been previously reported [1, 31].

The first specific discharge and charge capacities are 1,473 and 1,119 $mAhg^{-1}$ for urchin-like Fe_2O_3 and 1,325 and 1,068 $mAhg^{-1}$ for commercial Fe_3O_4. However, the specific capacities of both urchin-like Fe_2O_3 and commercial Fe_3O_4 fade quickly (Fig. 5a, b). Compared with urchin-like Fe_2O_3 and commercial Fe_3O_4, the first specific discharge capacity of Fe_3O_4/C composite is 1,260 $mAhg^{-1}$, as shown in Fig. 5c, which is much higher than its theoretical specific capacity (862.3 $mAhg^{-1}$). The extra discharge capacity may be attributed to the larger electrochemical active surface area and the formation of the SEI layer [5, 22]. The initial Coulombic efficiency of the Fe_3O_4/C composite is 86.8%, which is significantly higher than 76% of the urchin-like Fe_2O_3, 80.6% of the commercial Fe_3O_4 and most of the reported results [1, 2, 14, 30, 32], showing a remarkable decrease of the irreversible capacity loss. Since the second cycle, the Coulombic efficiency rapidly rises from 86.8% to 97.2% and then remains above 98% in the following cycles. Moreover, the Fe_3O_4/C composite exhibits a much better cycling performance than urchin-like Fe_2O_3 and commercial Fe_3O_4 (Fig. 5d). It can be seen that the specific discharge capacities of urchin-like Fe_2O_3 and commercial

Fig. 4 SEM images of **a** urchin-like Fe_2O_3 and **b** commercial Fe_3O_4
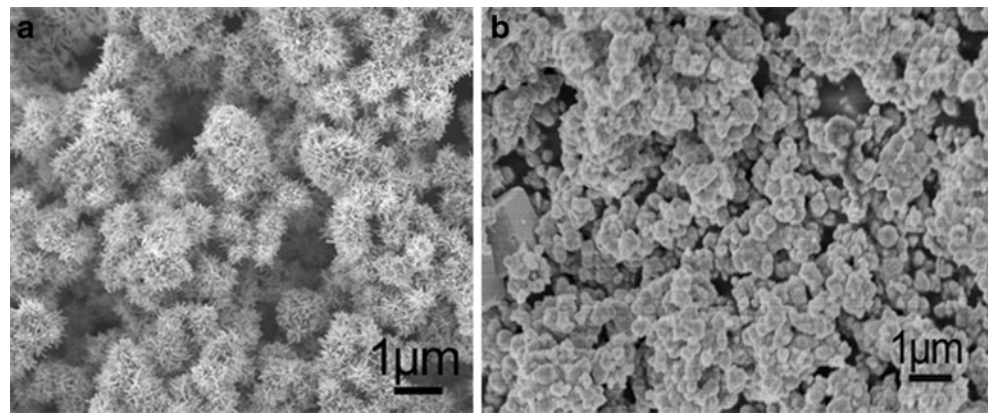
Fe_3O_4 decrease rapidly to 155 and 395 mAhg^{-1}, respectively, up to 50 cycles. In contrast, the specific discharge capacity of the Fe_3O_4/C composite decreases slightly and remains about 830 mAhg^{-1} after 50 cycles, which is almost 5.4 times of that of the urchin-like Fe_2O_3 and two times of that of the commercial Fe_3O_4. Moreover, even compared with the anode materials of carbon-coated Fe_3O_4 reported in the literatures [7, 11, 13, 14, 32–34], a better cycling performance is achieved in this paper.

Besides high capacity, rate capability is also important for high performance LIBs. Figure 6a shows the voltage profiles of the Fe_3O_4/C composite cycled at current rate from 0.1 to 2 C (1 C is defined as 8 Li$^+$/h). It can be seen that the composite delivers a discharge capacity of 1,152 mAhg^{-1} at a low current rate of 0.1 C. When the rate increases to 0.2 and 0.5 C, the discharge capacity decreases slowly to 1,009 and 917 mAhg^{-1}, respectively. Even at higher rates of 1 and 2 C, the composite can also
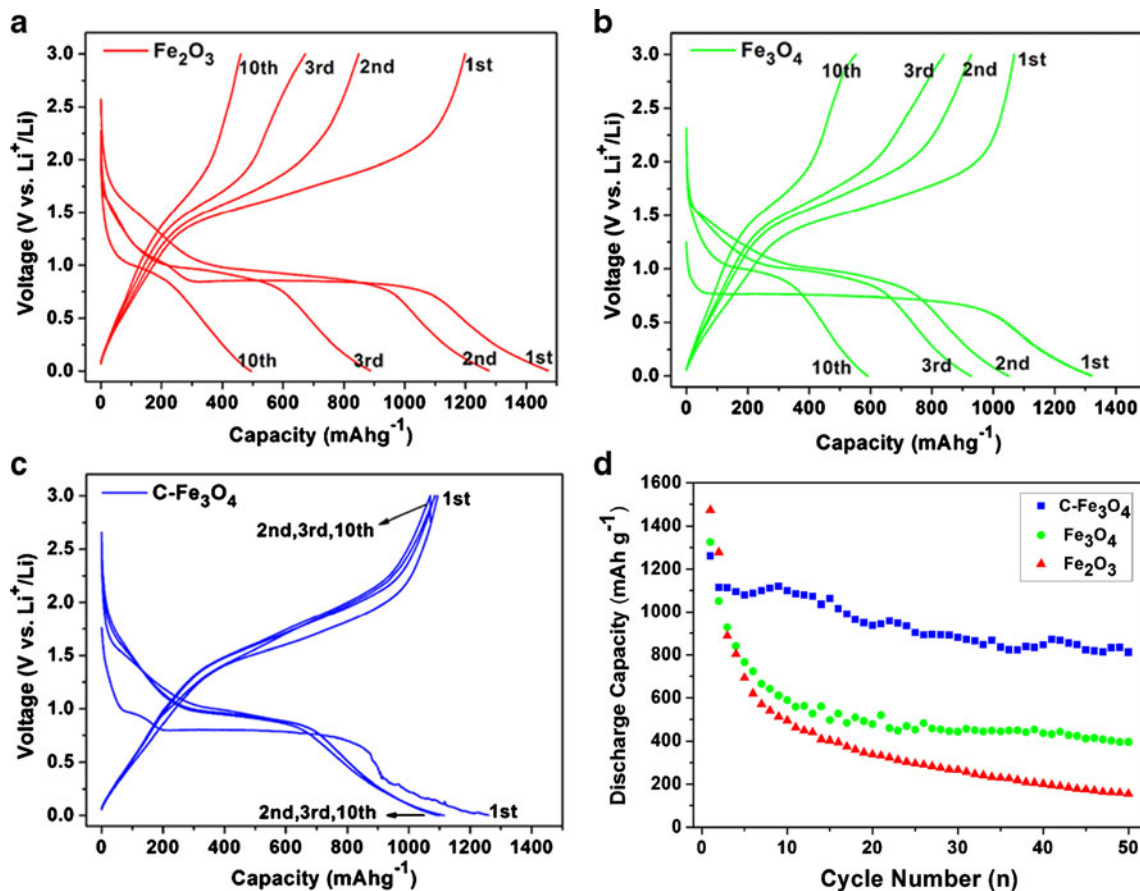

Fig. 5 Galvanostatic charge/discharge curves of **a** urchin-like Fe_2O_3, **b** commercial Fe_3O_4, and **c** the Fe_3O_4/C composite cycled at the first, second, third, and tenth between 3 and 0 V (vs. Li$^+$/Li) at a current rate of 0.1 C. **d** Comparison of the cycling performance of urchin-like Fe_2O_3, commercial Fe_3O_4, and Fe_3O_4/C composite
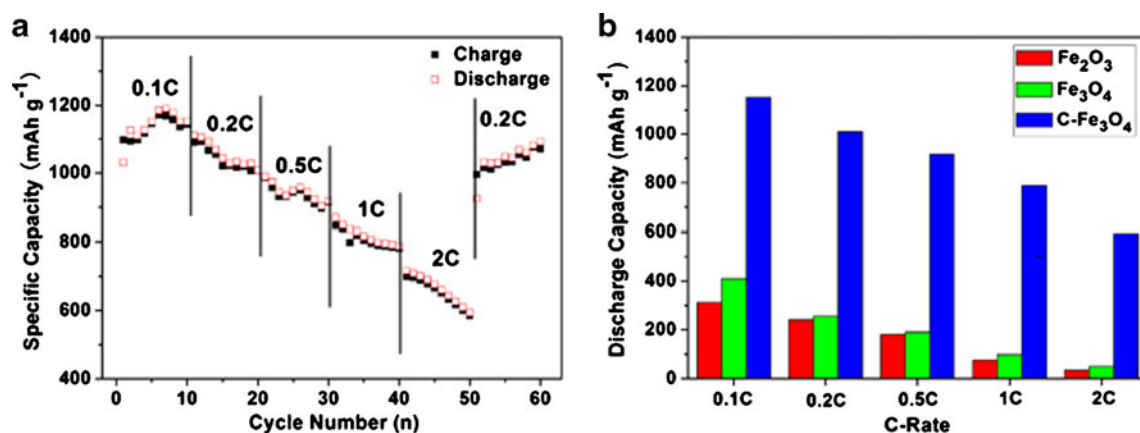
Fig. 6 **a** Rate capability of the Fe_3O_4/C composite at various current rate between 0.1 and 2 C. **b** Comparison of the rate performance of urchin-like Fe_2O_3, commercial Fe_3O_4, and Fe_3O_4/C composite

deliver a high capacity of 788 and 594 mAh g^{-1}, respectively, exhibiting a favorable high rate performance. Moreover, when the rate returns to 0.2 C after 50 cycles, the capacity can go back to more than 900 mAh g^{-1}, as illustrated in Fig. 6a, whereas the specific discharge capacities of urchin-like Fe_2O_3 and commercial Fe_3O_4 deliver poor capacity at low current rates and nearly no capacities at high rates (Fig. 6b). The results indicate the improved electrochemical performances of the Fe_3O_4/C composite in terms of cycling performance and rate capability.

Since the electrochemical performance is directly related to the impedance of the cells, the AC impedance of the as-prepared cells were characterized at the end of the discharge in some cycles during 0.1 C cycling processes. Figure 7a plots the AC impedance spectra of the (Fe_3O_4/C)/Li half cells after 1 and 50 cycles. We can see that the impedance spectra of the cell after one cycle is composed of two merged semicircles and a straight sloping line, which are corresponding to the resistance of the surface film, charge-

transfer resistance, and the Warburg impedance [2, 3, 10], whereas, the total resistance decreases substantially from 80 to 23 Ω after 50 cycles and the second semicircle disappears as the cycle number increases. This change is likely due to the so-called electrochemical milling effect reported before [2]. Figure 7b displays the impedance spectra of the cells based on the three kinds of materials after 50 cycles. The difference is clearly seen in that the resistance of Fe_3O_4/C composite (23 Ω) is smaller than those of urchin-like Fe_2O_3 (80 Ω) and commercial Fe_3O_4 (50 Ω), which indicates that the Li ions and electrons can transfer more easily across the composite/electrolyte interfaces, thus resulting in the enhanced electrode reaction kinetics and improved electrochemical performances.

We consider that the superior electrochemical performance combined with high reversible capacity, excellent cycle performance, and good rate capability could be associated with the combined advantages. Firstly, the mesoporous urchin-like composite randomly contacts with each other building up netlike macroporous electrode films.
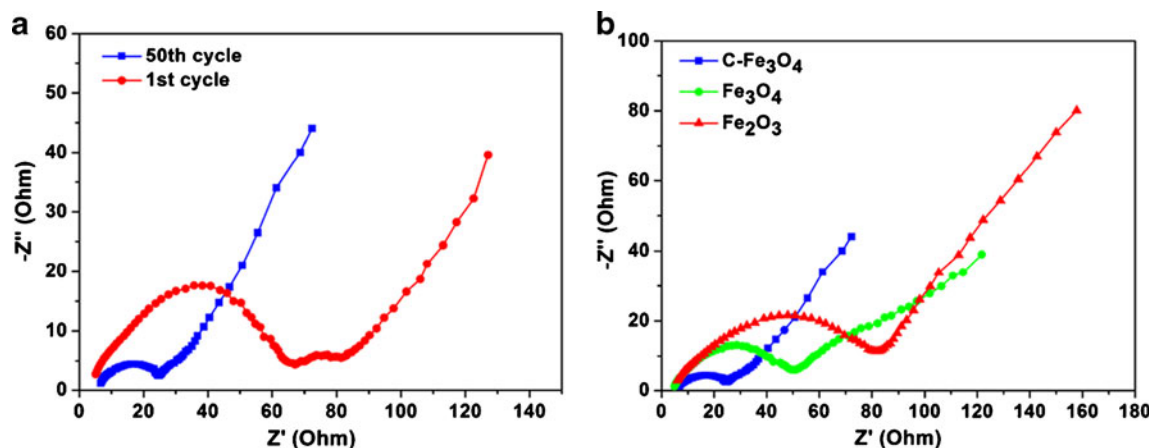

Fig. 7 **a** AC impedance spectra of Fe_3O_4/C composite at the open-circuit voltage after some electrochemical cycles. **b** Comparison of the AC impedance of urchin-like Fe_2O_3, commercial Fe_3O_4, and Fe_3O_4/C composite at the open-circuit voltage after 50 cycles

This opened porous structure facilitates electrolyte penetrate into inner regions of the films and every part of the composite [12, 35] and shortens diffusion paths for electrons/Li ions, which are beneficial for full utilization of active materials and account for the high reversible capacity and good rate capability. Secondly, the highly porous structure provides larger reaction surface and inner space favoring the efficient electrode/electrolyte interface contact, as well possesses more active sites for Li ions to enter [1, 10, 27]. Meanwhile, it is noted that porous structure also provides enough void spaces to buffer volume change and accommodate the strain associated with the volume variation, enhancing the cycle performance. Thirdly, the intriguing nano/micro-structured morphology also contributes to the improved electrochemical performance. The microscopic structure has a specific loose structure and provides a thermodynamically stable system, in which the mechanical stress caused by the severe volume change is sufficiently alleviated and the aggregation between the active materials is also prevented, whereas the nanometer-sized rods are able to reduce Li ion diffusion length. Furthermore, the carbon layer cannot only suppress the aggregation of the core magnetite nanocrystals during cycling but also act as electronic conductive channels to improve the electronic conductivity of Fe_3O_4. Therefore, the Fe_3O_4/C composite can be utilized beneficially during the conversion reaction with lithium, exhibiting superior electrochemical performances. We believe that this novel hybrid electrode can improve the intrinsic poor electronic kinetic, offering a new insight into fully exploits excellent electrochemical performances of Fe_3O_4 and other metal oxide anodes.

Conclusions

In summary, mesoporous nano/micro-structured Fe_3O_4/C composite has been successfully prepared. The urchin-like structure consisted of oriented mesoporous nanorods. When tested as the anode in LIBs, the Fe_3O_4/C composite exhibited a high reversible capacity, excellent cycling performance, and good rate capability. These superior electrochemical performances could be related to the synergistic effects of the nano/micro-structure, the porosity, and the carbon layer, which would jointly contribute to enhancing the structural stability and improving the lithium storage kinetics. The results indicate that this unique composite may find promising applications in high energy density or high power LIBs.

References

1. Ban C, Wu Z, Gillaspie D, Chen L, Yan Y, Blackburn J, Dillon A (2010) Adv Mater 22:E145
2. Wang S, Zhang J, Chen C (2010) J Power Sources 195:5379
3. Wang L, Yu Y, Chen PC, Zhang DW, Chen CH (2008) J Power Sources 183:717
4. Taberna P, Mitra S, Poizot P, Simon P, Tarascon J (2006) Nat Mater 5:567
5. Wu Z, Ren W, Wen L, Gao L, Zhao J, Chen Z, Zhou G, Li F, Cheng H (2010) ACS Nano 4:3187
6. Tarascon J, Armand M (2001) Nature 414:359
7. Zhang M, Lei D, Yin X, Chen L, Li Q, Wang Y, Wang T (2010) J Mater Chem 20:5538
8. Paek SM, Yoo EJ, Honma I (2009) Nano Lett 9:72
9. Xiang JY, Wang XL, Xia XH, Zhang L, Zhou Y, Shi SJ, Tu JP (2010) Electrochim Acta 55:4921
10. Wang C, Wang D, Wang Q, Chen H (2010) J Power Sources 195:7432
11. Cui Z, Jiang L, Song W, Guo Y (2009) Chem Mater 21:1162
12. Jiang J, Liu J, Ding R, Ji X, Hu Y, Li X, Hu A, Wu F, Zhu Z, Huang X (2010) J Phys Chem C 114:929
13. Zhang W, Wu X, Hu J, Guo Y, Wan L (2008) Adv Funct Mater 18:3941
14. Lee G, Park J, Sung Y, Chung K, Cho W, Kim D (2009) Nanotechnology 20:295205
15. Aricò A, Bruce P, Scrosati B, Tarascon J, van Schalkwijk W (2005) Nat Mater 4:366
16. Muraliganth T, Murugan A, Manthiram A (2009) Chem Commun 2009:7360
17. Chen J, Cheah Y, Chen Y, Jayaprakash N, Madhavi S, Yang Y, Lou X (2009) J Phys Chem C 113:20504
18. Zhan F, Geng B, Guo Y (2009) Chem Eur J 15:6169
19. Wang J, Du G, Zeng R, Niu B, Chen Z, Guo Z, Dou S (2010) Electrochim Acta 55:4805
20. Owens BB, Passerini S, Smyrl WH (1999) Electrochim Acta 45:215
21. Xu W, Canfield NL, Wang D, Xiao J, Nie Z, Zhang JG (2010) J Power Sources 195:7403
22. Liu S, Yin X, Chen L, Li Q, Wang T (2010) Solid State Sci 12:712
23. Yang R, Gu Y, Li Y, Zheng J, Li X (2010) Acta Mater 58:866
24. Pan Q, Qin L, Liu J, Wang H (2010) Electrochim Acta 55:5780
25. Wang X, Wu X, Guo Y, Zhong Y, Cao X, Ma Y, Yao J (2010) Adv Funct Mater 20:1680
26. Hao QY, Liu S, Yin XM, Du ZF, Zhang M, Li LM, Wang YG, Wang TH, Li QH (2010) CrystEngComm. doi:10.1039/C0CE00194E
27. Li Y, Tan B, Wu Y (2008) Nano Lett 8:265
28. Chun L, Wu X, Lou X, Zhang Y (2010) Electrochim Acta 55:3089
29. Liu H, Wang G, Park J, Wang J, Liu H, Zhang C (2009) Electrochim Acta 54:1733
30. Duan H, Gnanaraj J, Chen X, Li B, Liang J (2008) J Power Sources 185:512
31. Liu J, Li Y, Fan H, Zhu Z, Jiang J, Ding R, Hu Y, Huang X (2010) Chem Mater 22:212
32. He Y, Huang L, Cai J, Zheng X, Sun S (2010) Electrochim Acta 55:1140
33. Liu H, Wang G, Wang J, Wexler D (2008) Electrochem Commun 10:1879
34. Piao Y, Kim H, Sung Y, Hyeon T (2010) Chem Commun 46:118
35. Pan Q, Liu J (2009) J Solid State Electrochem 13:1591